

Gravity Wave Breaking over the Central Alps: Role of Complex Terrain

QINGFANG JIANG

University Corporation for Atmospheric Research, Monterey, California

JAMES D. DOYLE

Naval Research Laboratory, Monterey, California

(Manuscript received 4 April 2003, in final form 15 March 2004)

ABSTRACT

The characteristics of gravity waves excited by the complex terrain of the central Alps during the intensive observational period (IOP) 8 of the Mesoscale Alpine Programme (MAP) is studied through the analysis of aircraft in situ measurements, GPS dropsondes, radiosondes, airborne lidar data, and numerical simulations.

Mountain wave breaking occurred over the central Alps on 21 October 1999, associated with wind shear, wind turning, and a critical level with Richardson number less than unity just above the flight level (~ 5.7 km) of the research aircraft NCAR Electra. The Electra flew two repeated transverses across the Ötztaler Alpen, during which localized turbulence was sampled. The observed maximum vertical motion was 9 m s^{-1} , corresponding to a turbulent kinetic energy (TKE) maximum of $10.5 \text{ m}^2 \text{ s}^{-2}$. Spectrum analysis indicates an inertia subrange up to 5-km wavelength and multiple energy-containing spikes corresponding to a wide range of wavelengths.

Manual analysis of GPS dropsonde data indicates the presence of strong flow descent and a downslope windstorm over the lee slope of the Ötztaler Alpen. Farther downstream, a transition occurs across a deep hydraulic jump associated with the ascent of isentropes and local wind reversal. During the first transverse, the turbulent region is convectively unstable as indicated by a positive sensible heat flux within the turbulent portion of the segment. The TKE derived from the flight-level data indicates multiple narrow spikes, which match the patterns shown in the diagnosed buoyancy production rate of TKE. The turbulence is nonisotropic with the major TKE contribution from the v -wind component. The convectively unstable zone is advected downstream during the second transverse and the turbulence becomes much stronger and more isotropic.

The downslope windstorm, flow descent, and transition to turbulence through a hydraulic jump are captured by a real-data Coupled Ocean–Atmosphere Mesoscale Prediction System (COAMPS) simulation. Several idealized simulations are performed motivated by the observations of multiscale waves forced by the complex terrain underneath. The simulations indicate that multiscale terrain promotes wave breaking, increases mountain drag, and enhances the downslope winds and TKE generation.

1. Introduction

Turbulent breakdown of mountain waves has been the subject of numerous studies during the last 3 decades because of its potential hazard to aircraft, role in global momentum balance, and connection to strong surface windstorms over mountain lee slopes. Mountain wave breaking may occur associated with backward wind shear, decrease of air density with altitude, or high terrain, under which conditions waves may steepen and overturn (e.g., Hines 1968). The aircraft in situ observation of the well-known Boulder windstorm on 11 January 1972, obtained during the Colorado Lee Wave Observational Project, established the relationship between gravity wave breaking aloft and the surface windstorm

in the lee (Lilly and Zipser 1972; Lilly and Kennedy 1973). This study inspired numerous theoretical studies for several decades. Even today these observations remain the most detailed available for large-amplitude wave breaking. Early studies of windstorm dynamics focused on the nonlinear response of an idealized atmospheric state to two-dimensional bell-shaped terrain. This included numerical simulations, such as Klemp and Lilly (1978), Clark and Peltier (1977), Peltier and Clark (1979, 1983), and Durran (1986); analytical formulation using Long's equation (Long 1953), such as Smith (1985); and laboratory experiments (Rottman and Smith 1989). Although some details of the dynamical mechanisms are still debated (e.g., Lilly and Klemp 1980; Peltier and Clark 1980), the relationship between wave breaking aloft and the windstorm at the surface has been well established. The wave breaking–induced turbulent region could serve either as an internal boundary to reflect wave energy downward to cause resonance, or

Corresponding author address: Qingfang Jiang, UCAR Visiting Scientist, NRL, 7 Grace Hopper Ave., Monterey, CA 93943-5502.
E-mail: jiang@nrlmry.navy.mil

Report Documentation Page				Form Approved OMB No. 0704-0188	
Public reporting burden for the collection of information is estimated to average 1 hour per response, including the time for reviewing instructions, searching existing data sources, gathering and maintaining the data needed, and completing and reviewing the collection of information. Send comments regarding this burden estimate or any other aspect of this collection of information, including suggestions for reducing this burden, to Washington Headquarters Services, Directorate for Information Operations and Reports, 1215 Jefferson Davis Highway, Suite 1204, Arlington VA 22202-4302. Respondents should be aware that notwithstanding any other provision of law, no person shall be subject to a penalty for failing to comply with a collection of information if it does not display a currently valid OMB control number.					
1. REPORT DATE 15 MAR 2004		2. REPORT TYPE		3. DATES COVERED 00-00-2004 to 00-00-2004	
4. TITLE AND SUBTITLE Gravity Wave Breaking over the Central Alps: Role of Complex Terrain				5a. CONTRACT NUMBER	
				5b. GRANT NUMBER	
				5c. PROGRAM ELEMENT NUMBER	
6. AUTHOR(S)				5d. PROJECT NUMBER	
				5e. TASK NUMBER	
				5f. WORK UNIT NUMBER	
7. PERFORMING ORGANIZATION NAME(S) AND ADDRESS(ES) Naval Research Laboratory, 7 Grace Hopper Ave., Stop 2, Monterey, CA, 93943-5502				8. PERFORMING ORGANIZATION REPORT NUMBER	
9. SPONSORING/MONITORING AGENCY NAME(S) AND ADDRESS(ES)				10. SPONSOR/MONITOR'S ACRONYM(S)	
				11. SPONSOR/MONITOR'S REPORT NUMBER(S)	
12. DISTRIBUTION/AVAILABILITY STATEMENT Approved for public release; distribution unlimited					
13. SUPPLEMENTARY NOTES					
14. ABSTRACT					
15. SUBJECT TERMS					
16. SECURITY CLASSIFICATION OF:			17. LIMITATION OF ABSTRACT Same as Report (SAR)	18. NUMBER OF PAGES 18	19a. NAME OF RESPONSIBLE PERSON
a. REPORT unclassified	b. ABSTRACT unclassified	c. THIS PAGE unclassified			

as an interface for hydraulic flow that becomes supercritical flow over the lee slope. The sensitivity of down-slope windstorms to the asymmetry of mountain profiles has been examined by Miller and Durran (1991). They found that steep lee slopes tend to promote wave breaking. Three-dimensional aspects of wave breaking have been examined by Clark and Farley (1984) and more recently by Clark et al. (1994) and Afanasyev and Peltier (1998).

The study of gravity wave breaking has also been fueled by the discovery that momentum deposition associated with gravity wave breaking in the middle atmosphere is necessary to balance mean Coriolis torque driven by radiative cooling in the polar regions (e.g., Leovy 1964; Lindzen 1981; Holton 1982). The importance of appropriate drag parameterization associated with mountain wave breaking in global circulation models is illustrated in more recent studies (e.g., Kim et al. 2003). The interaction between waves, critical levels, wave breaking, and mean flow has been the subject of numerous studies (e.g., Fritts 1978; Durran 1995). More detailed reviews of the subject can be found in Fritts and Alexander (2003) and Kim et al. (2003).

While a great deal has been learned from idealized numerical studies, the modeling of wave breaking is known to be sensitive to the parameterization of sub-grid-scale turbulence and surface processes. For example, the 1972 Boulder windstorm has recently been revisited by Doyle et al. (2000) in a model intercomparison study. Although the 11 mesoscale models show some similar skill in capturing the low-level hydraulic jump and wave breaking aloft, the details of the solutions differ significantly among the models. Unless reliable direct numerical simulation can be performed, field observations are still critical in order to establish the relevancy between wave breaking in nature and in numerical models. However, while mountain gravity wave breaking is three-dimensional in nature, conventional observational tools can only record data in one dimension. Recent advances in remote sensing technology provide powerful tools for the observations of three-dimensional turbulence and the structure of topographically forced flows (Ralph and Neiman 1997; Clark et al. 2000; Smith et al. 2002). In general, well-documented observations of wave breaking are still rare.

Understanding gravity waves excited by complex terrain and associated wave breaking is one of the primary objectives of the Mesoscale Alpine Programme (MAP; Bougeault et al. 2001). Although mesoscale models frequently forecasted large-amplitude or breaking gravity waves during the special observational period (SOP) of MAP, the case presented here was one of the few missions that the aircraft-sampled turbulence possibly related to mountain wave breaking. The Boulder windstorm has been the subject of numerous studies in which the Rocky Mountain Front Range was represented by a smooth bell-shaped hill. Unlike the relatively simple terrain shape of the Front Range, the complex terrain

of the Alps is multiscale and three-dimensional in character. Little is known about the interaction of waves excited by multiscale terrain and its influence on wave breaking. The objective of this study is to further our understanding of gravity wave breaking over complex terrain through observational data analysis, real-data simulation, and idealized numerical experiments.

The remainder of this paper is organized as follows. A brief overview of the synoptic conditions and the observations is given in section 2. Section 3 provides an analysis of the wind and stability profiles using three soundings. Waves and hydraulic jumps are discussed in section 4 based on the analysis of flight-level data, scanning aerosol backscatter lidar (SABL) imagery, and global positioning system (GPS) dropsonde data. Section 5 includes spectral analysis and estimation of vertical fluxes and turbulent kinetic energy using aircraft in situ measurements. In section 6, the Coupled Ocean–Atmosphere Mesoscale Prediction System (COAMPS) real-data simulation is compared with observations. The role of multiscale terrain in wave breaking is further investigated in section 7 through a series of two-dimensional idealized simulations. Section 8 contains conclusions.

2. Synoptic overview

On 21 October 1999, a southerly foehn developed over the Alps associated with the approach of a deep cyclone from the west (Fig. 1). A high pressure ridge was located over the eastern Alps, which advected warm air from the south across the Alps. Over the central Alps, the wind speed was approximately 20 m s^{-1} at 500 hPa. Precipitation to the south of the Alps, and gravity waves and secondary potential vorticity (PV) banners to the north of the Alps were forecasted in advance by a number of mesoscale models [Swiss Model, French Aire Limitée Adaptation Dynamique Développement International (ALADIN), Canadian Mesoscale Compressible Community (MC2), Naval Research Laboratory (NRL) COAMPS, etc.] In the early morning of 21 October, the National Center for Atmospheric Research (NCAR) Electra research aircraft, equipped with flight-level instruments, GPS dropsondes, and down-looking SABL, flew missions in support of three dry MAP objectives: gap flow, gravity wave breaking, and secondary PV banners.

The NCAR Electra departed from the Innsbruck airport at 0604 UTC and executed two repeated transverses across the Ötztaler Alpen and the Inn Valley between 0648 and 0749 UTC in order to sample gravity waves. The flight altitude was approximately 5.7 km MSL and the transverses were aligned along the wind direction (see Fig. 2 for the terrain and flight track). Each transverse is approximately 160 km long with a flight endurance of 30 min. While the Ötztaler range is a highly three-dimensional section of the main Alpine chain, there are several quasi-two-dimensional ridges and val-

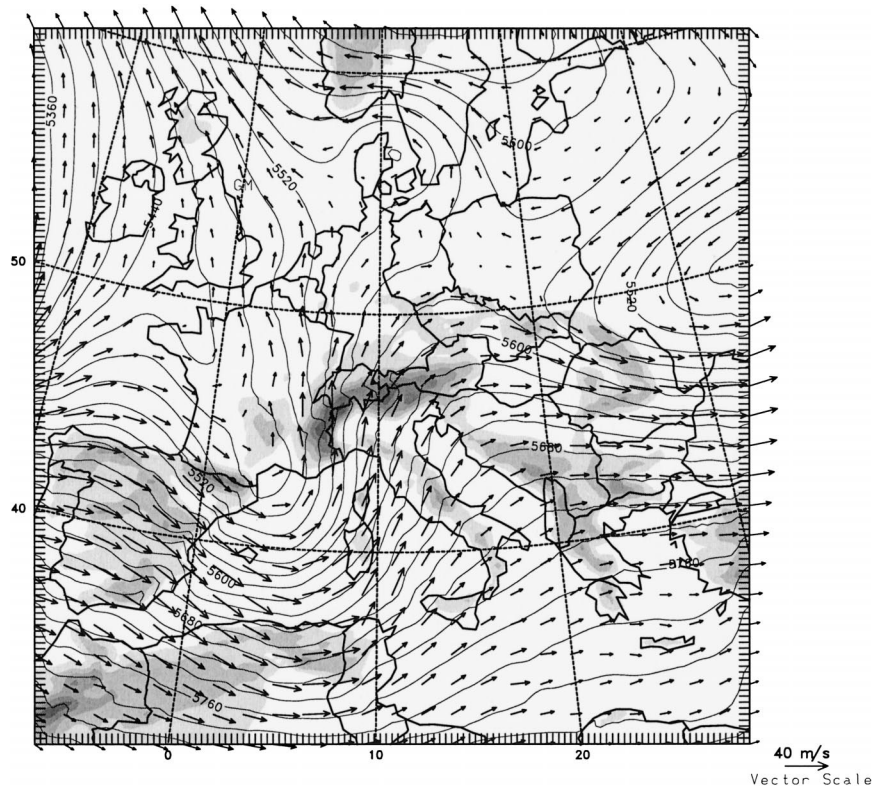


FIG. 1. Synoptic conditions over Europe on the 500-hPa surface valid at 0600 UTC 21 Oct 1999, derived from the COAMPS 27-km mesh grid. Wind vectors and geopotential height contours (contour interval = 50 m) are shown. Terrain is represented by the grayscale.

leys beneath the flight track (Fig. 2). The major ridges or peaks include (from south to north) Ortles (3905 m MSL), Palla Bianca (3738 m MSL), and Wildspitze (3768 m MSL). The major valleys include (Fig. 2, from south to north) Val Venosta (in Italy), Pitztal, Ötztal, and Inn Valley. Turbulence was encountered during both transverse approximately between 46.9° – 47.5° N (Fig. 2, indicated by Δ). Several sharp spikes in vertical motion were recorded. Eleven GPS dropsondes were successfully deployed with a relatively uniform spacing along the two transverse, and additionally, the SABL instrument provided information about clouds and aerosols.

3. Vertical profiles

To understand the vertical structure of the ambient flow and its evolution, the vertical profiles of wind speed, wind direction, v -wind component, potential temperature, relative humidity, and Richardson number are plotted in Fig. 3. The profiles are derived from three soundings launched from two nearby stations, Innsbruck and Vipiteno. Innsbruck (47.26° N, 11.355° E; 579 m MSL) is located in the Inn Valley and is closest to the flight track (Fig. 2). A radiosonde was launched from Innsbruck at 0600 UTC 21 October 1999, that is, about 30 min before the aircraft measurements. However, as

will be shown, the Innsbruck sounding is not necessarily representative of the upstream flow because it was modified by the descent in the lee of high peaks such as Habicht (3277 m MSL) and possibly turbulent mixing associated with wave breaking. Nevertheless, the 0600 UTC sounding at Innsbruck is plotted in Fig. 3 for reference. Vipiteno/Sterzing (46.89° N, 11.44° E; 942 m MSL) is located approximately 50 km to the east of the flight track (Fig. 2). The neighboring terrain is relatively low (<2 km) in this region. Therefore, Vipiteno/Sterzing is considered a better representation of the upstream flow. Two radiosondes were launched from Vipiteno/Sterzing at 0600 and 0900 UTC 21 October 1999, respectively.

The Vipiteno/Sterzing 0600 UTC sounding reveals a low-level jet between 3 and 5 km with an average wind speed of 18 m s^{-1} , and a reversed wind shear between 5 and 8 km. The jet stream is located at 12 km MSL with a wind speed maximum of 28 m s^{-1} . Between 2 and 6 km, the wind direction is primarily southerly, with an average directional shear of $10^{\circ} \text{ km}^{-1}$. A stronger directional shear is evident around the 6-km level, where the wind direction changes from 200° at 6 km to 250° at 7 km. The v -wind component reaches 19 m s^{-1} at 6 km and decreases to zero at the 8-km level, indicative of a critical level for meridional propagating waves. The potential temperature profiles indicate that the air is

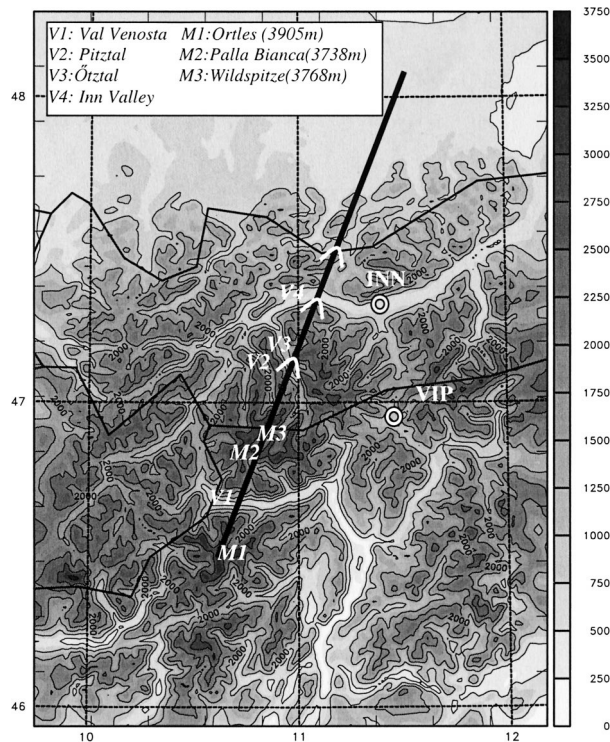


FIG. 2. The topography of the central Alps (m) in the COAMPS fourth grid mesh. The solid lines represent the political boundaries. The thick solid line indicates the location of the NCAR Electra flight segment with \wedge representing regions where turbulence was encountered during the flight. Key geographic points of interests are labeled. Two relevant sounding stations, Innsbruck (INN) and Vipiteno (VIP), are indicated by white circles.

moderately stable in the lowest 4–5 km with a less stable layer above. The air is near saturation below 4 km and is drier aloft. The Richardson number is approximately 3 below 3 km, decreases to 2 in the 3–5-km layer, and further decreases to unity at the 6-km level. The 0900 UTC sounding indicates a fairly rapid change of wind speed during the 3-h period. The low-level jet becomes stronger (maximum $\sim 22 \text{ m s}^{-1}$) with time, and the directional shear above the jet is lower in altitude ($\sim 5.2 \text{ km}$) and greater in magnitude ($\sim 80^\circ$ over a 300-m vertical distance). The air in the 4–8-km layer is significantly drier, likely associated with flow descent. A critical level with respect to the v -wind component descends to 5.6 km MSL accordingly.

In summary, the soundings at Vipiteno reveal the existence of a critical level in the middle troposphere just above the NCAR Electra flight level associated with both backward shear in the wind speed and directional turning. The corresponding Richardson number is less than unity near the critical level. It is known from previous studies that the presence of a critical level, small Richardson number, and backward shear promotes wave breaking. The unsteadiness of the large-scale flow is also evident, likely associated with the passage of the warm front (Fig. 1).

4. Waves, turbulence, and hydraulic jump

a. Vertical displacement and SABL

Considering that the flight was approximately along the wind direction, the vertical displacement of air parcels can be derived from aircraft data assuming a steady state and using

$$\eta(x) = \int_0^x (w'/U) dx, \quad (1)$$

where $w'(x) = w(x) - \bar{w}$ and U is the along-flight track wind component. The reference point ($x = 0$) corresponds to the beginning points of each leg. A Lanczos filter has been applied with a high pass of 200 m and a low pass of 100 km. The backscatter from the Electra lidar (SABL) along the first transverse is plotted in Fig. 4 along with the vertical displacement $\eta(x)$ derived from the in situ aircraft data using Eq. (1). The corresponding terrain underneath the flight segment is shown at the bottom. The terrain is bilinearly interpolated to the aircraft position from a 100-m resolution digital terrain dataset. The multiscale nature of the terrain along the flight track is evident. At least two dominant horizontal scales can be seen; the $\sim 100\text{-km}$ scale corresponding to the envelope of the main Alpine ridge and the 10–30-km scale corresponding to isolated peaks and valleys.

There are two well-defined waves over the lee of Wildspitze with a maximum peak-to-trough amplitude (PTA) of 0.5 km and a wavelength of approximately 11 km. Another wave with a similar wavelength and a plateau-like peak is located between 47.1° and 47.2°N , which is probably either highly nonlinear or breaking. Further downstream, there are several small-amplitude waves ($\text{PTA} < 0.3 \text{ km}$) with shorter wavelengths (6 \sim 8 km). The strong SABL return aloft is apparently associated with liquid water in clouds. The wave troughs and cloud-free gaps match each other reasonably well. The SABL return also indicates that the altitude of the cloud top decreases from 5.5 to 3.5 km within about 20-km horizontal distance downstream of Wildspitze (over Pitztal). This type of spectacular “waterfall” downstream of major peaks has been observed during several MAP gravity wave IOPs (e.g., Smith et al. 2002; Doyle and Smith 2003; Volkert et al. 2003). It is clearly an indication of strong flow descent, likely associated with a downslope windstorm. There is an approximately 20-km-wide cloud-free gap located farther downstream. Clouds reappear downstream of Pitztal, indicating the return of isentropes to their original level.

To the north of the Alps ($\sim 47.7^\circ\text{N}$), the SABL backscatter indicates a shallow high-concentration aerosol layer (200 \sim 300 m deep) with a flat top, which likely corresponds to the boundary layer top. The high aerosol concentration within the boundary layer was also observed during the second transverse (Fig. 5), as well as the flight transverses that sampled secondary potential vorticity banners along the north side of the Alps. Data

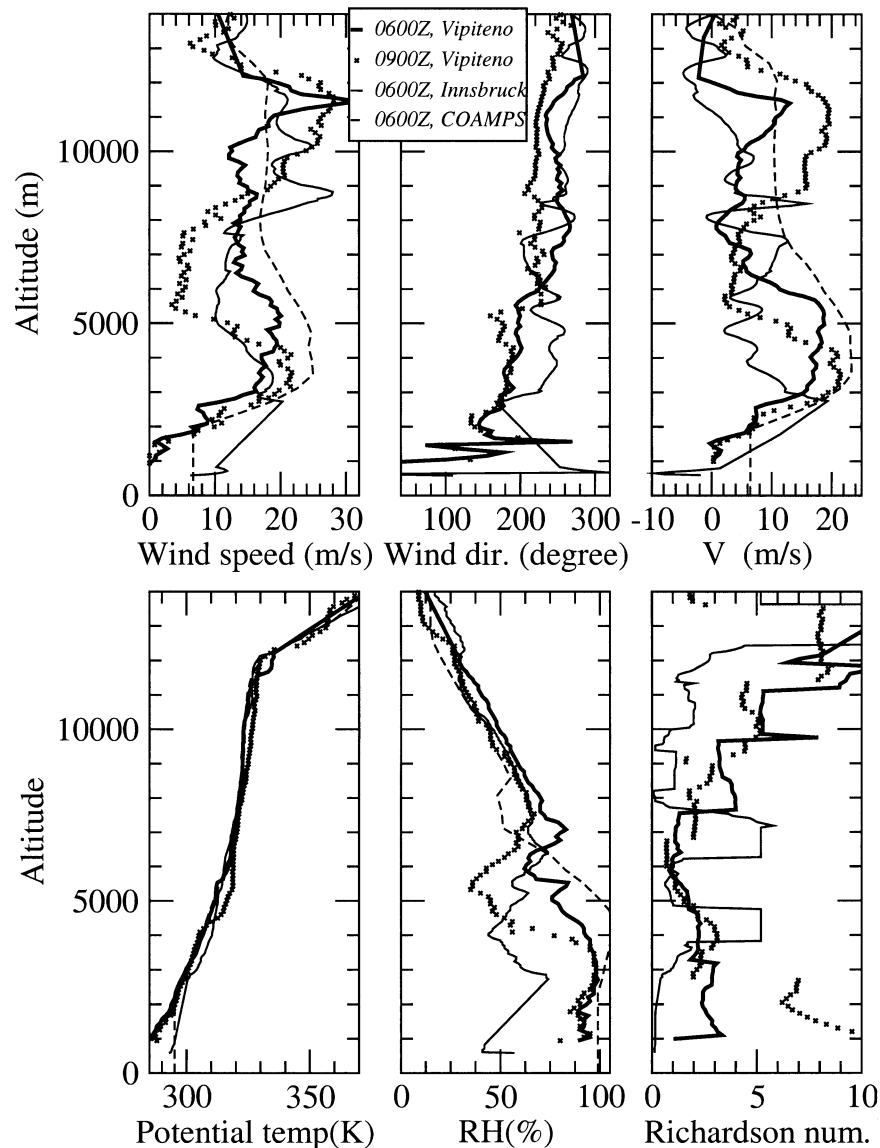


FIG. 3. Profiles derived from the 0600 and 0900 UTC Vipiteno and 0600 UTC Innsbruck soundings. The following quantities are plotted: wind speed (m s^{-1}), wind direction (deg), meridional wind component (m s^{-1}), potential temperature (K), relative humidity (%), and Richardson number. Profiles of wind speed, v component, potential temperature, and relative humidity derived from the innermost grid mesh of the COAMPS simulation located approximately at the Vipiteno sounding location are plotted for comparison.

derived from GPS dropsondes deployed to the north of the Alps indicates that the air in the boundary layer is much colder and drier than the air above; evidence that the air is likely stagnant. The southerly foehn only reaches the ground over a short distance (to the south of 47.7°N in Fig. 4 and to the south of 47.8°N in Fig. 5).

Figure 5 shows the SABL backscatter and the vertical displacement along the second transverse. The terrain along the two legs match each other well. However, the overall SABL backscatter patterns and vertical displacement curves are substantially different. Similarly, there are two laminarlike waves over the lee of Wildspitze,

but the wave amplitude is much larger during the second transverse ($\text{PTA} \sim 0.8 \text{ km}$). Vertical motions between 47° and 47.6°N show strong nonlinearity, as indicated by the two very sharp-peaked waves between 47.1° and 47.4°N , probably associated with breaking mountain waves. Several short waves ($\leq 10 \text{ km}$) are apparent further downstream.

b. Analysis of GPS dropsonde data

Within a time period of 1 h, 11 GPS dropsondes were deployed along the two transverses, which provide valu-

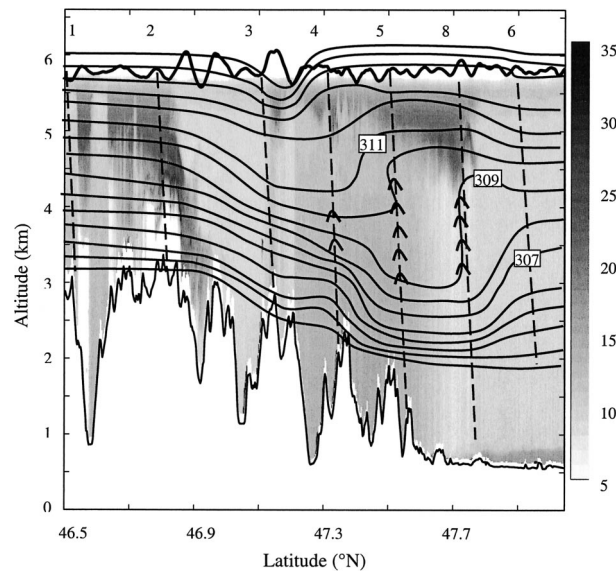


FIG. 4. The SABL backscatter coefficient (in grayscale), vertical displacement (thick solid curve between 5–6 km), and potential temperature contours (solid, interval = 1 K) along the first transverse. The vertical displacement is computed from the flight-level winds using Eq. (1). The potential temperature is derived from GPS dropsondes (see text for details). The dashed lines are GPS dropsonde trajectories and the dropsondes are numbered sequentially in time. The symbol ^ indicates turbulent regions above the boundary layer. The terrain along the flight track is shown along the bottom.

able documentation of the wind, stratification, and turbulence below the flight level. A manual analysis of the potential temperature, along-flight track component of the wind, and turbulence kinetic energy ($TKE = u'^2/2 + v'^2/2 + w'^2/2$) in the vertical section along the two flight segments is shown in Figs. 4–7 with the corre-

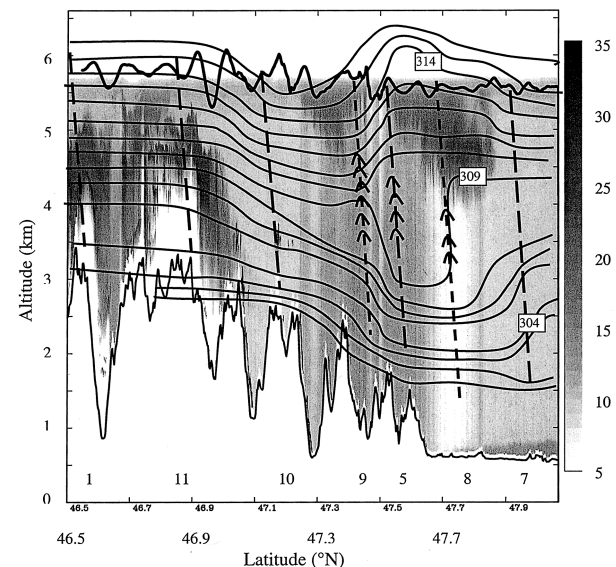


FIG. 5. Same as Fig. 4, except for the second transverse. The dropsondes used are numbered along the abscissa.

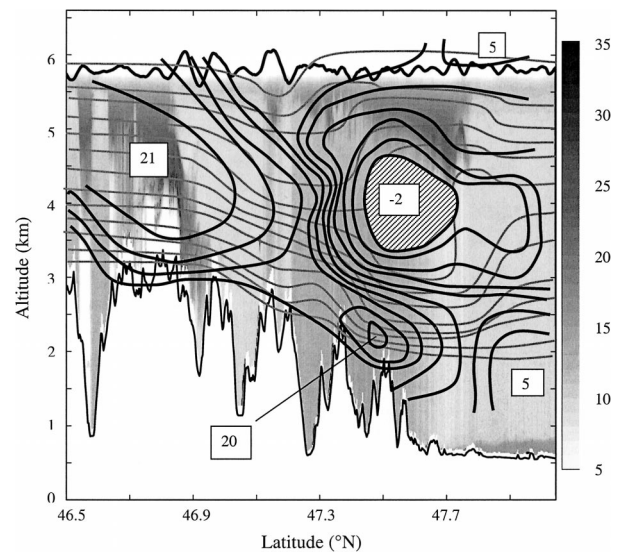


FIG. 6. Same as Fig. 4, except the isentropes are shown in gray and the along-flight track wind component in black contours (interval = 2 m s^{-1}). The wind maxima and minima are labeled. The region with reversed wind is hatched.

sponding SABL backscatter. The turbulent kinetic energy (TKE) is computed using a discrete Fourier transform (DFT) filter, and scales smaller than 250 m in the vertical direction are considered turbulent perturbations. The results are relatively insensitive to this cutoff scale. The regions with TKE above $0.2 \text{ m}^2 \text{ s}^{-2}$ are indicated by symbol ^. Seven dropsondes (numbers 1–6 and 8 for the first leg and numbers 1, 5, and 7–11 for the second leg) and the corresponding flight-level data are used for the analysis, which results in a horizontal resolution of about 20–40 km. Smaller-scale features such as the ~ 10 -km waves observed in the vertical displace-

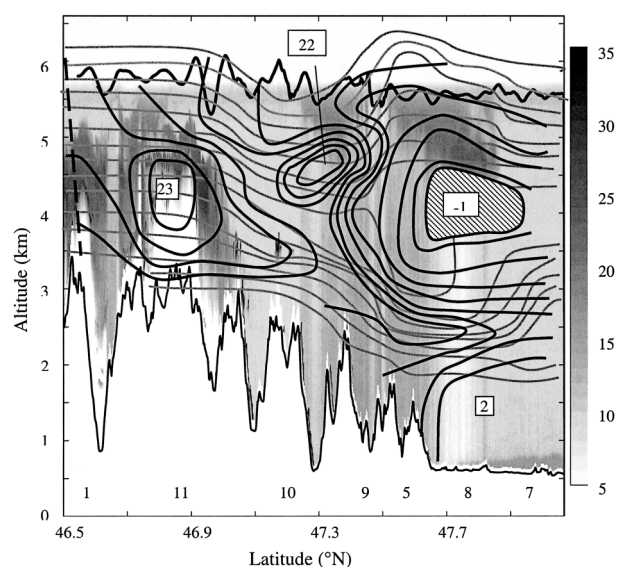


FIG. 7. Same as Fig. 6, except for the second transverse.

ment field are not resolved in this analysis. The approximate descent paths of the dropsondes are indicated by dashed lines in Figs. 4 and 5.

Figure 4 indicates persistent flow descent between 46.6° and 47.2°N , which is consistent with the wide cloud gap over Fundusfeiler and Ötztal indicated by the SABL backscatter. Downstream of 47.2°N , the isentropes 313–316 K recover to their upstream altitudes, which is consistent with the reappearance of the clouds observed by the SABL. Farther downstream, a hydraulic jump is evident with steepened isentropes and TKE near 4 km MSL. At 47.5°N , a superadiabatic layer exists between 3–5 km. The phase line of the steepened isentropes tilts upstream with height as observed in many numerical simulations and some observations (e.g., Doyle et al. 2000). The along-flight track component of the horizontal wind is shown in Fig. 6. The wind contours indicate the existence of strong downslope flow with a maximum wind speed of 21 m s^{-1} . A sharp shear zone is evident, located approximately between 3 and 4.5 km MSL where the wind speed drops from 14 m s^{-1} to zero in a distance of 20 km along the flight track, associated with the occurrence of a hydraulic jump. Weak wind reversal exists between 47.4° and 47.7°N . Directly beneath the reversal zone, wind speed reaches a second maximum at the 2-km level. The transition of the low-level flow (in the lowest 2.5 km) from strong downslope winds to weak flow occurs at 47.7°N associated with the ascent of isentropes. The analysis for the second transverse is shown in Figs. 5 and 7. While the dominant features such as severe winds, hydraulic jump, and wind reversal are generally similar, the evolution of flow structure over 30 min is nevertheless striking. For example, the ascent of the 313–316-K isentropes shifts approximately 20 km downstream. Correspondingly, the cross-mountain wind component reversal zone advects downstream as well (Fig. 7). A wind maximum now appears at 47.3°N and between 4 and 5.2 km. The downstream movement of the jump revealed by the GPS dropsonde analysis is consistent with the cloud-clear patterns observed by SABL.

5. Spectra, TKE, and fluxes

a. Spectra analysis

Two flight-level in situ datasets are available; one is 1-Hz low-frequency data with dozens of variables and the other is 25-Hz data of the three wind components. The mean aircraft speed was 140 m s^{-1} . Therefore, the corresponding spatial resolution is approximately 140 m for the 1-Hz data and 5.6 m for the 25-Hz data.

As an example, several variables from the low-frequency data are plotted in Fig. 8. The southerly wind is fairly strong ($\sim 20 \text{ m s}^{-1}$) upstream of 46.9°N , and becomes much weaker downstream. The v component approaches zero around 47.2° and 47.45°N . In fact, the high-frequency data recorded negative v at the two lo-

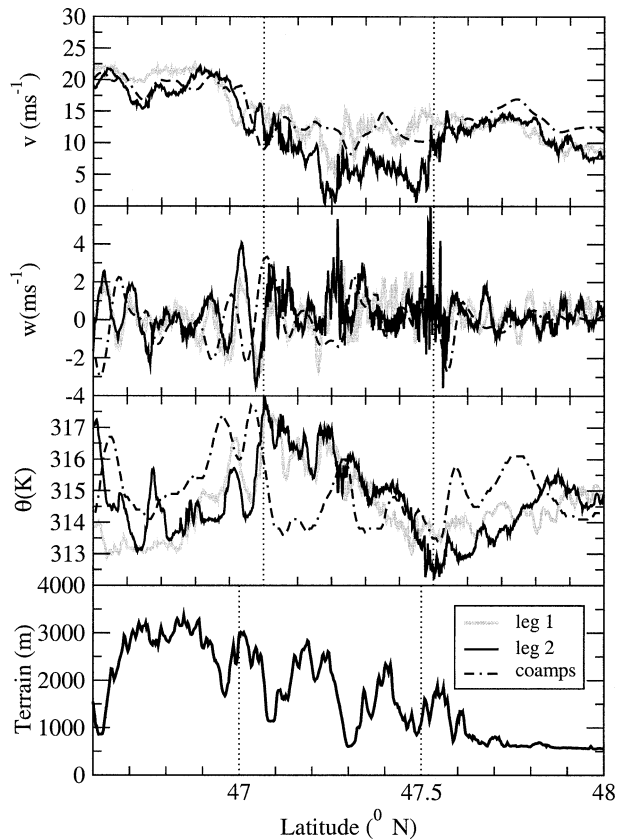


FIG. 8. The plot of two wind components (i.e., v and w), and potential temperature (K) vs the latitude ($^\circ\text{N}$) from flight-level data and COAMPS. The gray curves are for the first transverse and the dark curves for the second. Dotted-dashed curves are derived from the COAMPS simulation. The corresponding terrain (m) along the first transverse is included for reference.

cations. There are two waves upstream of 47°N (see the plot of w), with a maximum vertical motion of 2.2 m s^{-1} for the first leg and 4.5 m s^{-1} for the second leg. Comparing with the relatively smooth waves upstream, the vertical motion between 47° and 47.6°N is much more turbulent. Along the second transverse, a narrow maximum in the vertical motion is approximately located at 47.2°N , where the vertical motion reaches 5.2 m s^{-1} . There are three local maxima near 47.5°N with a maximum w of 6 m s^{-1} . According to the high-frequency data, the maximum vertical motion for the first transverse is 3.9 (around 47.2°N) and 9.0 m s^{-1} for the second leg (around 47.5°N). In addition to the small-scale waves (11 km or less), the potential temperature plot indicates a larger-scale response: a warming (descent), cooling (ascent), and warming (descent) pattern with a wavelength of approximately 100 km. The turbulence encountered during the flight is located over the cooling (ascent) limb of the long wave. In general, the horizontal wind is about 20% stronger during the second transverse.

Figure 9 shows the power spectrum density (PSD) of

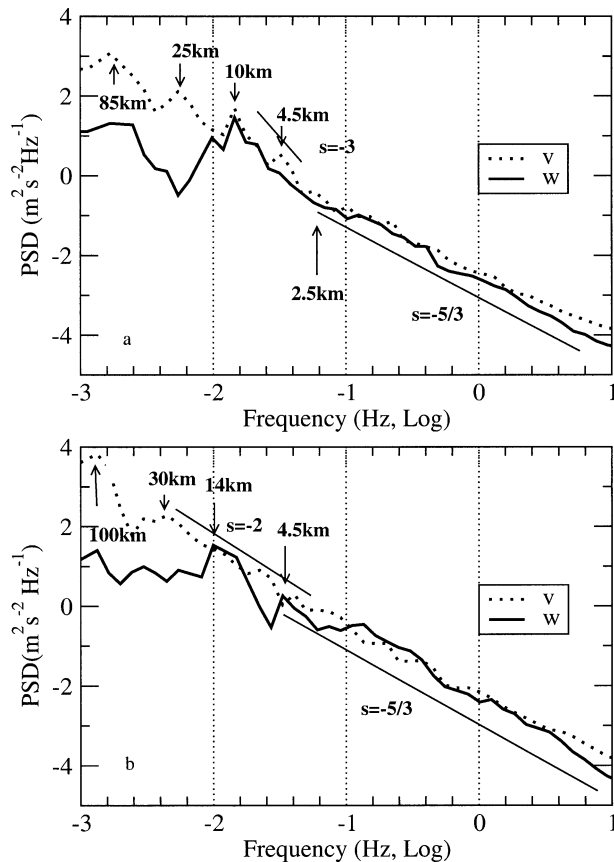


FIG. 9. The power spectra density of v and w vs sampling frequency derived from the 25-Hz data are plotted in log coordinates for (a) transverse 1 and (b) transverse 2. The wavelengths corresponding to some peaks in the spectra are labeled.

v and w computed from the high-frequency data in log-log coordinates. The data have been linearly detrended before applying a DFT. The computed spectra have been smoothed through equal log intervals. The horizontal axis is labeled as the log of sampling frequency (in Hertz). For the first transverse, the spectrum of v exhibits the characteristic $-5/3$ slope for scales smaller than 2.5 km (Fig. 9a). Four distinctive energy-containing peaks are located at 85, 25, 11, and 4.5 km, respectively. The slope between 3- and 11-km wavelength is approximately -3 . The spectrum of the vertical wind component is characterized by a peak near 11 km and a possible inertia subrange up to 5 km, with a slope of $-5/3$. The spectra for wavelengths between 5–11 km are characterized by a slope of -3 as well. The peak at 11 km apparently corresponds to the relatively long waves observed in the vertical displacement (see Figs. 4–7). A broad peak is located between 50 and 85 km. Although the 85-km peak in the spectrum may not be statistically significant because of the limited length of the flight transverse, nevertheless, it is consistent with the large-scale variation of the potential temperature (Fig. 8), likely associated with inertia-gravity waves in response to

the main Alpine ridge forcing. Comparing with the v spectrum, the peaks at 25 and 4.5 km are absent from the w spectrum. If the peak at 4.5 km in the v spectrum corresponds to eddies generated by breaking mountain waves, the absence of such a peak in the w spectrum implies that the eddies are not isotropic.

The spectra for the second transverse are shown in Fig. 9b. Again, we observe an inertia subrange up to ~ 5 km in both the w and v spectra. The spectrum of v shows two major peaks approximately corresponding to 30- and 100-km scales, respectively. There are smaller peaks with scales less than 8 km, likely corresponding to eddies associated with breaking mountain waves. The average slope between 5–30-km wavelengths is approximately -2 . The w spectrum shows three major peaks, located at 100, 14, and 4.5 km, respectively. Compared with the w spectrum of transverse 1, the shift of the 11-km peak to 14 km suggests a possible upscale transport of wave energy associated with wave breaking.

b. Fluxes

The vertical fluxes of the two horizontal momentum components $\rho w' u'$ and $\rho w' v'$, where u' , v' , and w' are velocity perturbations, and sensible heat $c_p \rho w' \theta'$, where $c_p = 1004 \text{ J K}^{-1} \text{ kg}^{-1}$, and θ' is the potential temperature perturbation, along the two transverse are shown in Figs. 10 and 11. In each panel, there are two curves representing contributions from small-scale ($L < 5$ km) and larger-scale ($5 \text{ km} < L < 20$ km) perturbations, respectively. Contributions from scales larger than 20 km have been filtered. We refer to perturbations with horizontal scales less than 5 km as turbulence and in the 5–20-km range as waves for the convenience of description. Again, DFT has been employed for scale separation. The overbar represents a moving average over 10 km. It should be noted that due to the low moisture content at the flight level, $c_p \rho w' \theta' \approx c_p w' \theta'_v$, where θ'_v is virtual potential temperature perturbation. Therefore, only $c_p \rho w' \theta'$ is shown.

Figures 10 and 11 indicate that momentum and heat fluxes are dominated by the contributions from wave-scales. During the first transverse, the zonal momentum flux due to wave-scale perturbations shows a 25-km-wide positive maximum centered at 47°N , indicating an upward transfer of the zonal momentum. The meridional momentum flux shows a pair of minima centered approximately at 46.98° and 47.18°N . The first peak coincides with the maximum in zonal momentum flux, but with an opposite sign. The contribution from turbulence is much smaller. The alternating positive and negative peaks in the turbulence-scale momentum flux indicate that the local vertical wind shear is controlled by relatively small-scale wave dynamics. The wave-scale sensible heat flux shows a major peak centered at 47°N with a maximum of 320 W m^{-2} . For a linear wave in a stably stratified flow, with the vertical motion and potential temperature perturbations in quadrature, the

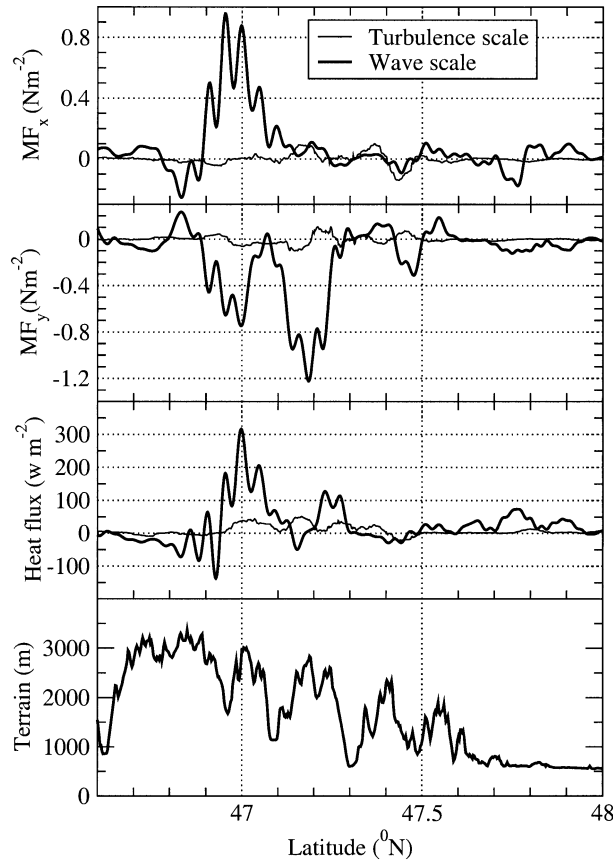


FIG. 10. The momentum and heat fluxes along the first transverse are plotted. Contributions from both wave and turbulent scales are included. The horizontal axis is the sampling latitude. The corresponding terrain is plotted for reference.

vertical heat flux should be zero. Although there are several waves upstream of 46.9°N , the heat flux is almost zero, indicating that the waves upstream of 46.9°N are likely quasi linear. In contrast, the net upward flux between 46.9° and 47.3°N indicates that the wave-scale motion is nonlinear or turbulent in that region. The vertical heat flux due to turbulence is positive between 46.9° and 47.4°N , indicative of convective instability. There are three 15–40-km-wide peaks and the maximum value is about 40 W m^{-2} . The heat flux is downward between 47.4° and 47.5°N .

Along the second transverse (Fig. 11), the wave-scale vertical flux of the zonal momentum shows a positive maximum centered at 46.95°N . Again, the contribution from the turbulence scale is generally much smaller except for between 47.3° and 47.5°N , where both wave- and turbulent-scale fluxes are negative and comparable. The vertical flux of the wave-scale meridional momentum shows a major negative peak at 46.95°N . The negative correlation between the zonal and meridional momentum fluxes may be related to the directional shear in the ambient flow, that is, at the flight level, $\partial u/\partial z > 0$ and $\partial v/\partial z < 0$. The contribution from turbulence is

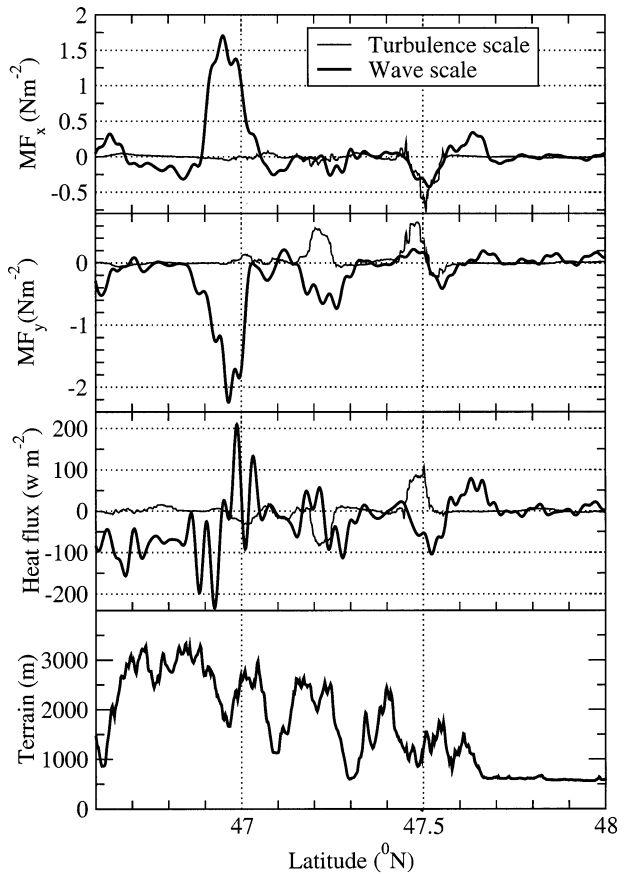


FIG. 11. Identical to Fig. 10, except for the second transverse.

about 20% of that from waves. Lilly and Kennedy (1973) computed the horizontal momentum fluxes using flight-level data sampled over the Front Range of the Colorado Rockies during the 1970 Colorado Lee Wave Program. According to their calculation, the amplitude of momentum flux averaged over individual flight track is of the order of 0.5 Pa below 15 km MSL. There is a turbulent layer between 15 and 17 km, above which the momentum flux decreases to zero rapidly. Georgelin and Lott (2001) computed the horizontal momentum flux associated with lee waves over the Pyrénées during the intensive observation period (IOP 3) of the Pyrénées Experiment (PYREX). Their flight track-averaged horizontal momentum flux is approximately 1.2 Pa below 5 km and 0.4 Pa in the upper troposphere. Averaging the wave-scale momentum flux over individual flight segments, we obtain the two momentum flux components (MF_x and MF_y), which are 0.08 and -0.16 Pa for the first leg and 0.075 and -0.18 Pa for the second leg. These values are comparable with the momentum fluxes above the turbulent layer computed by Lilly and Kennedy (1973).

The sensible heat flux along the second transverse differs significantly from that observed along the first transverse. On the turbulence scale, the heat flux be-

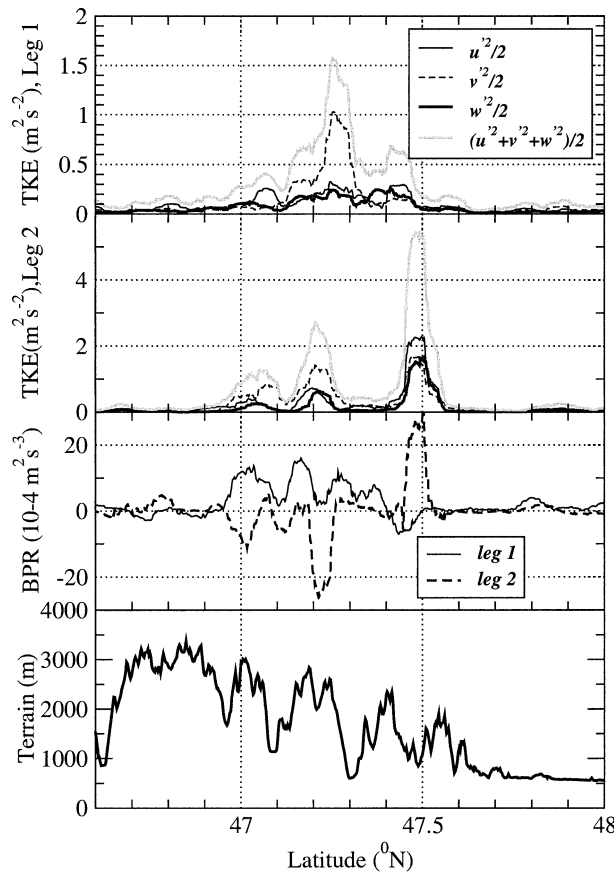


FIG. 12. TKE and the buoyancy production rate (BPR) of TKE along the two transverse as a function of the latitude. Terrain along the first transverse is plotted for reference.

tween 46.9°–47.3°N is primarily negative indicating that the air is stable. A narrow positive maximum of 100 W m^{-2} is centered at 47.5°N, probably associated with the development of the hydraulic jump shown in section 4.

c. Turbulent kinetic energy

The TKE is computed using a DFT filter and shown in Fig. 12. Only contributions from scales smaller than 5 km are included. The choice of the cutoff scale (i.e., 5 km) is based on the observation of the power spectra of v and w . There is a gap approximately at the wavelength of 6 km in both the v spectrum for the first leg and the w spectrum of the second leg. The variation of the computed TKE is less than 15% when the cutoff scale is changed to 4 or 6 km. If we consider a model grid mesh with 1-km increments as applied in this study, the minimum resolvable scale is at best 4 km. Turbulence processes with scales smaller than 4 or 5 km must be represented by the “subgrid” TKE parameterization. Therefore, the choice of a 5-km cutoff scale is consistent with the model grid 4 mesh resolution. A moving average is applied to the computed TKE.

Along the first transverse, three distinctive local TKE

maxima exist between 46.9° and 47.5°N with the maximum centered at 47.25°N (Fig. 12). The major contribution comes from the meridional component (i.e., $v'^2/2$). The contribution from $w'^2/2$ is much smaller, an indication of nonisotropy of the turbulence, and consistent with the spectra in Fig. 9. The tripeak structure is more distinct during the second transverse. The major peak is located at 47.5°N with a maximum of $5.5 \text{ m}^2 \text{ s}^{-2}$, which is significantly larger than observed along the first transverse. The maximum TKE computed using high-frequency data is $10.5 \text{ m}^2 \text{ s}^{-2}$ along the second leg. The turbulence is more isotropic along the second leg relative to the first leg. The downstream drift of the turbulence maximum is consistent with the vertical section analysis of the GPS dropsonde data.

If we ignore the advection, vertical divergence of the TKE flux and isotropic terms, and use the Boussinesq approximation, the TKE budget equation can be written as (Karacas and Marwitz 1980)

$$\frac{\partial e}{\partial t} = -\frac{\overline{u'w'}}{\rho} \frac{\partial u}{\partial z} - \frac{\overline{v'w'}}{\rho} \frac{\partial v}{\partial z} + \frac{g}{\theta} \overline{w'\theta'} - \epsilon, \quad (2)$$

where the first two terms on the right-hand side represent the shear generation rates of TKE, the third term is the buoyancy generation rate of TKE, and the last term is the energy cascade rate. The TKE budget can be estimated from the flight-level data and the radiosondes. In turbulence inertial subrange, the power spectrum satisfies the Kolmogorov law:

$$E(f) = \alpha(\text{TAS})^{2/3}(2\pi)^{-2/3}\epsilon^{2/3}f^{-5/3}, \quad (3)$$

where $\alpha = 0.5$ for the vertical motion spectrum, $\text{TAS} \approx 140 \text{ m s}^{-1}$ is the true aircraft speed, and f is the sampling frequency in Hertz. Using Eq. (3) and Figs. 9a and 9b, we estimate a mean dissipation rate $\epsilon \approx 8 \times 10^{-6} \text{ m}^2 \text{ s}^{-3}$ for the first transverse, and $\epsilon \approx 1.6 \times 10^{-5} \text{ m}^2 \text{ s}^{-3}$ for the second transverse. Using the small-scale heat fluxes, the buoyancy TKE production rate is computed using Eq. (2) and plotted in Fig. 12. Along the first transverse, buoyancy tends to produce TKE between 46.95° and 47.4°N and consume TKE between 47.4° and 47.5°N. Four spikes are present with a maximum TKE creation rate of $2.2 \times 10^{-3} \text{ m}^2 \text{ s}^{-3}$, which is two orders of magnitude larger than the dissipation (or cascade) rate ϵ .

For the first transverse, the correspondence between the buoyancy production rate and the TKE patterns is evident, indicating that the turbulence is still in a process of development. Along the second transverse, the TKE is much larger than observed during the first transverse. Between 46.9° and 47.4°N, the buoyancy production of TKE is negative, indicating that the turbulence is fully developed and decaying (Fig. 12). However, corresponding to the major peak at 47.5°N, the buoyancy production rate reaches a maximum of about $3 \times 10^{-3} \text{ m}^2 \text{ s}^{-3}$, an indication of vigorous turbulence development.

Due to the lack of direct measurements of the vertical

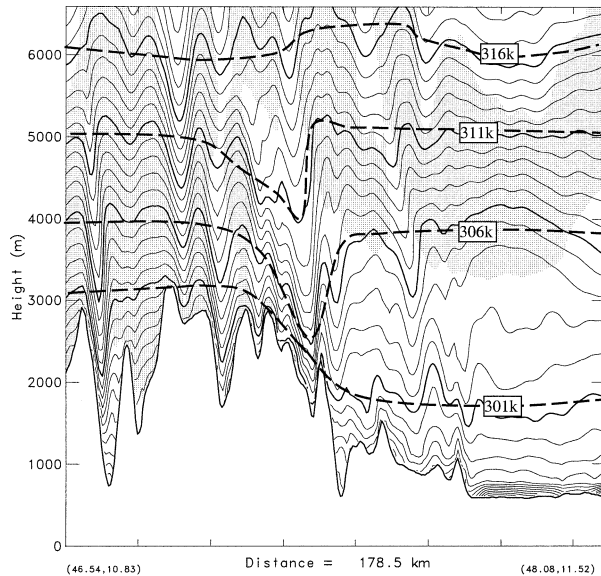


FIG. 13. Vertical sections of potential temperature (contour interval = 1 K) located approximately along the first transverse, valid at 0630 UTC 21 Oct 1999, derived from the fourth grid mesh of COAMPS real-data simulation. The isentropes of 301, 306, 311, and 316 K are manually smoothed (dashed curves). Areas with relative humidity larger than 85% are filled with dots.

shear, it is difficult to estimate the shear contribution. Using the Vipiteno 0600 UTC sounding, we estimate $\partial \bar{u} / \partial z \approx 0.0033 \text{ s}^{-1}$ and $\partial \bar{v} / \partial z \approx -0.00028 \text{ s}^{-1}$ at the 5.7-km level. Applying Eq. (2) and using the mean shear and turbulence-scale momentum fluxes, we find that for the second transverse, the shear production of TKE is of the same order as buoyancy contribution. For the first transverse, however, the shear production terms have both positive and negative contributions. The presence of both positive and negative values in the shear terms illustrates the difficulty in defining the mean vertical shear in wave breaking zones above complex terrain. For small-scale eddies, the mean vertical shear could be dominated by local wave activity.

6. Numerical simulations

The atmospheric component of the U.S. Navy's COAMPS (Hodur 1997) is used to simulate this southerly foehn event. COAMPS is a fully compressible, non-hydrostatic model with physical parameterizations, such as a 1.5-order TKE closure (Mellor and Yamada 1974) and cloud microphysics.

The computational domain for the present study is comprised of four horizontally nested grids of 121×121 , 112×136 , 136×160 , and 181×253 points. The corresponding horizontal spatial resolutions (Δx) are 27, 9, 3, and 1 km, respectively. The topographic data is taken from a 1-km digital elevation model (DEM) dataset. The terrain from the fourth mesh is shown in Fig. 2. There are 55 vertical levels and the

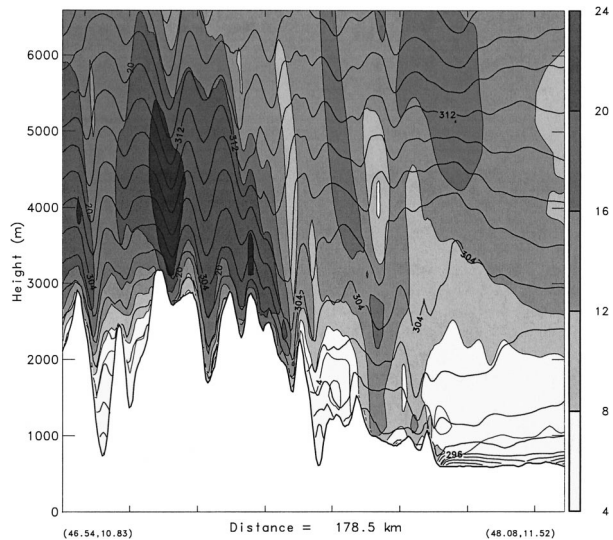


FIG. 14. Vertical sections of the v component of the wind (grayscale, interval = 4 m s^{-1}), located approximately along the first transverse, valid at 0630 UTC 21 Oct 1999, derived from the fourth grid mesh of COAMPS real-data simulation.

terrain-following coordinate is stretched with $\Delta Z_{\min} = 20 \text{ m}$ near the surface. A radiation boundary condition is applied at the model top. The lateral boundary conditions are specified using the Naval Operational Global Atmospheric Prediction System (NOGAPS) analyses and forecasts at a 6-h interval. An incremental update data assimilation procedure is used for the model initialization, which enables mesoscale phenomena to be retained in the analysis increment fields.

The southerly wind component (i.e., v), vertical motion (i.e., w), and potential temperature derived from the COAMPS simulation valid at 0700 UTC 21 October 1999 are included in Fig. 8 for comparison with flight-level measurements. The COAMPS data are interpolated to the aircraft position. In general, the observed and simulated v -wind component agree with each other reasonably well. For vertical motion, both the observations and the simulation indicate the presence of gravity waves upstream of 47°N . However, there appears to be a 90° phase difference between the observation and the simulation. Small differences between the model and real terrain fields and also reasonably small errors in the simulated winds likely contribute to the simulated vertical velocity errors. The simulated potential temperature tends to show an ascent, descent, and ascent pattern on a larger scale ($\sim 100 \text{ km}$) as observed.

Figures 13 and 14 show the model-predicted potential temperature, relative humidity, and v -wind component along a vertical section approximately oriented with the first flight transverse, valid at 0630 UTC. A cross section oriented along the second transverse valid at 0730 UTC is shown in Figs. 15 and 16. The underlying terrain is quite different from the interpolated terrain shown in Figs. 4–7, likely due to the coarser model resolution

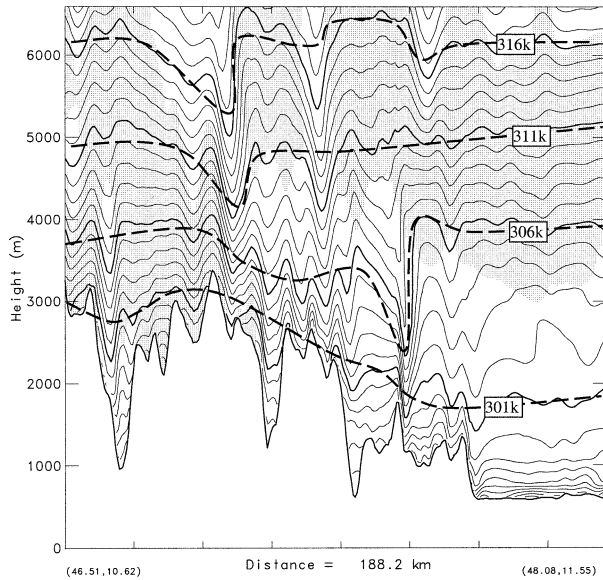


FIG. 15. Same as Fig. 13, except for a section corresponding to the second transverse and valid at 0730 UTC 21 Oct 1999.

and small deviations of the true flight track from a straight line.

The COAMPS vertical cross sections indicate the presence of short waves with wavelengths of the order of 10–20 km as shown in the vertical displacement in Figs. 4–7, which is not resolved by the dropsonde data due to the much coarser horizontal resolution. For the convenience of qualitative comparison, manually smoothed contours for $\theta = 301, 306, 311, 316$ K are included as dashed lines in Figs. 13 and 15. In general, COAMPS is successful in capturing relatively large-scale features, such as strong flow descent over the lee of Wildspitze associated with the formation of a cloud gap or foehn window (see the relative humidity patterns in Figs. 13 and 15) and the downslope windstorm. For example, the 316-K isentrope exhibits a descent–ascent–descent pattern, which is qualitatively in agreement with the dropsonde data. The COAMPS prediction agrees with the dropsonde observations fairly well in terms of the location and strength of the downslope windstorm. Downstream of the foehn window, a hydraulic jump occurs associated with a sharp recovery of the isentropic displacements (e.g., 306- and 311-K contour lines in Fig. 13) and a transition from strong downslope winds to relatively weak winds (Fig. 14). Figure 16 indicates that the vertical motion is stronger at the flight level at 0730 UTC than 1 h earlier, and the hydraulic jump is stronger as well. Both sections show a wind reversal in the Inn Valley in agreement with the 0600 UTC Innsbruck sounding.

The discrepancy between the observations and COAMPS forecast is also readily apparent. The simulated hydraulic jump is much weaker and the weak wind region downstream of the hydraulic jump is substantially smaller compared with the observations. The ob-

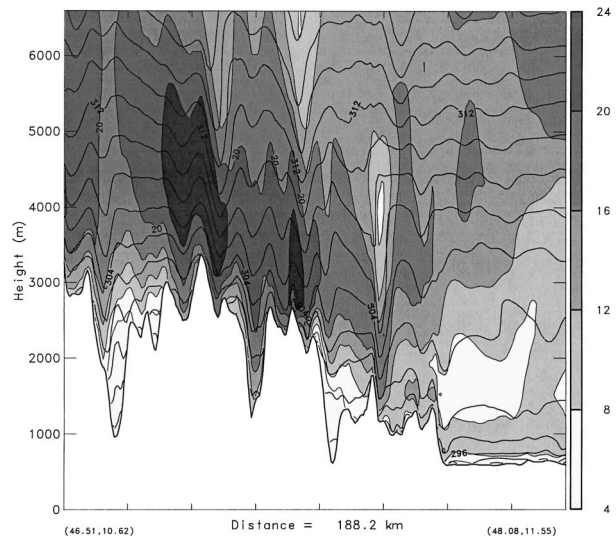


FIG. 16. Same as Fig. 14, except for a section corresponding to the second transverse and valid at 0730 UTC 21 Oct 1999.

served local wind reversal and unstable region associated with the jump is absent from the COAMPS forecast. This discrepancy is likely associated with the overforecast of wind speed, especially u -wind component in the midtroposphere. Although, COAMPS predicted reverse shear above the 5-km level, as shown in Fig. 3, the shear is not as strong as observed by the 0600 UTC Vipiteno sounding and no mean-state critical level is present with regard to u . Idealized two-dimensional simulations using the the 0600 UTC Vipiteno sounding and a sounding derived from the COAMPS simulation near Vipiteno demonstrate that the wind error lead to greater wave energy propagation into the upper troposphere. As a result, wave breaking in the lower and middle troposphere is not as vigorous as observed.

7. Wave breaking over multiscale terrain

The multiscale nature of the terrain along the flight track is evident in both the plan view (Fig. 2) and the vertical section plots (Figs. 4–7). The PSD of the interpolated terrain along the flight track is shown in Fig. 17. There are four major peaks in the PSD, approximately corresponding to 6-, 11-, 25-, and >70-km wavelengths, respectively. In comparison with Fig. 9, there appears to be a general correspondence between the terrain and the flight-level w spectra. Apparently, the airflow aloft responded to both the large-scale (>70 km) and smaller-scale (<25 km) forcing.

A multiscale wave response is also apparent in the analysis of the vertical displacement, flight-level TKE and fluxes, and GPS dropsonde data. For example, the vertical displacement indicates waves of a characteristic 10 km or smaller scale, and the cross sections constructed using dropsonde data show flow descent and ascent on a much larger scale. The TKE segment derived

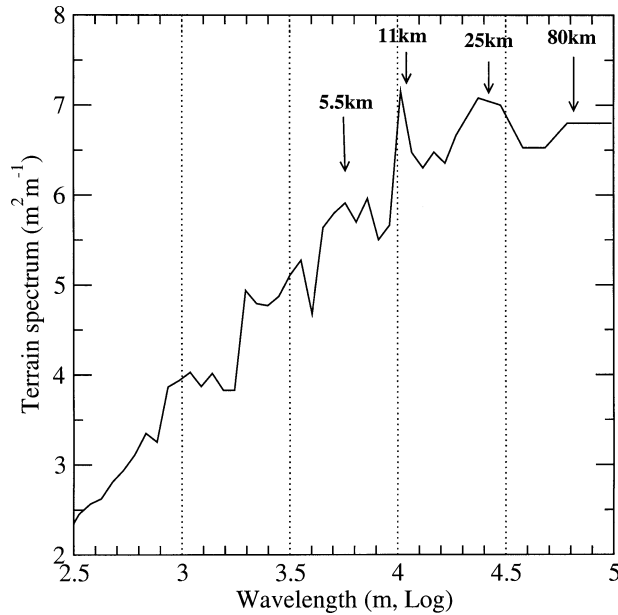


FIG. 17. The spectrum of terrain beneath the first flight segment as a function of wavelength.

from the flight in situ measurements is about 70 km long, while the width of individual TKE spikes is only approximately 25 km.

An important scientific question that arises from these observations is related to the role of the smaller-scale terrain in the initiation, evolution, and subsequent turbulence breakdown of gravity waves, which are addressed in the following subsections.

a. Idealized simulations

In most idealized studies of wave breaking over terrain, the underlying terrain is represented by simple shapes (such as Gaussian shape or “Witch of Agnesi”) with a dominant horizontal length scale. However, the spectra of complex terrain such as the Alps, the Andes, or Rockies are almost continuous, indicative of the multiscale nature of the orography. Little is known about the influence of multiscale terrain on the large-scale flow, especially in terms of wave breaking and drag. Motivated by the correspondence between observed multiscale wave response and the complex terrain underneath, we have conducted a number of two-dimensional idealized simulations using COAMPS to examine the impact of multiscale terrain on wave breaking. For simplicity, moist processes, rotation, bottom friction, and radiation are not taken into account in these idealized simulations.

The model is initialized using the Vipiteno 0600 UTC sounding. The cross-mountain wind speed is specified using the v -wind component. The two-dimensional terrain is described by the following equation:

$$h(x) = \begin{cases} 0, & \text{for } r > 1 \\ \frac{h_m}{1 + (x/a)^2}(1 - r), & \text{for } x < 0 \text{ and } r < 1 \\ \frac{h_m}{1 + (x/a)^2}(1 - r) + h_s \left[\cos\left(\frac{2k\pi x}{a}\right) - 1 \right], & \text{for } x > 0 \text{ and } r < 1, \end{cases} \quad (4)$$

where a is the large-scale mountain width, the factor $r = |x|/2a$ specifies the mountain range, h_m and h_s are mountain heights for the large- and smaller-scale terrain, and k is the nondimensional wavenumber of the smaller-scale terrain. Equation (4) represents a modified bell-shaped terrain with smaller-scale features superposed on the lee slope. The mountain is located in the center of a 1000-km-long domain with radiation lateral boundary conditions applied to the zonal direction boundaries and periodic conditions applied in the meridional direction. The horizontal resolution is 1 km. There are 90 levels in the vertical with a radiation boundary condition applied at the model top.

A number of simulations have been performed using $h_m = 2000$ m and $a = 70$ km, for a range of k and h_s . The potential temperature, wind speed, and turbulence kinetic energy at $t = 1.5$ and 3 h are shown in Figs. 18 and 19 for the two simulations with $h_s = 0$, and $h_s = 300$ m, $k = 2$, respectively.

For $h_s = 0$, a signature of breakdown of the long wave is indicated by the TKE maximum ($\approx 2 \text{ m}^2 \text{ s}^{-2}$) and wind reversal just below the critical level at $t = 1.5$ h (Fig. 18a). Beneath the wave breaking region, the downslope winds reach a maximum of 30 m s^{-1} approximately at the 2.5-km level. The wave perturbations are much smaller above the critical level (i.e., the 6-km level). At $t = 3$ h, the turbulence becomes much stronger and the wave breaking region becomes much deeper (Fig. 18b). A highly turbulent zone is located along the steep jumplike wave front. The TKE zone is vertically oriented with a maximum value of $36 \text{ m}^2 \text{ s}^{-2}$. A second TKE maximum is located in the main wave trough. The strongest downslope wind core is located directly beneath the two TKE maxima where the wind speed reaches 36 m s^{-1} . This simulation captures some common features of observed breaking waves. For example, it shows a sequence of turbulence development as observed in this case: TKE first appears near the mountain peak and then a narrow vertically oriented TKE cluster develops associated with a propagating hydraulic jump at a lower level (see Figs. 4–7 for comparison). The vertical section at $t = 3$ h also shows a backward tilt of phase line, wave breaking aloft and a hydraulic jump downstream (Fig. 18b).

Figure 19 shows the corresponding pair of plots for $h_s = 300$ m and $k = 2$ (i.e., wavelength equals 35 km). At $t = 1.5$ h, wave breaking is well developed as indicated by a deep TKE cluster with a maximum of 18

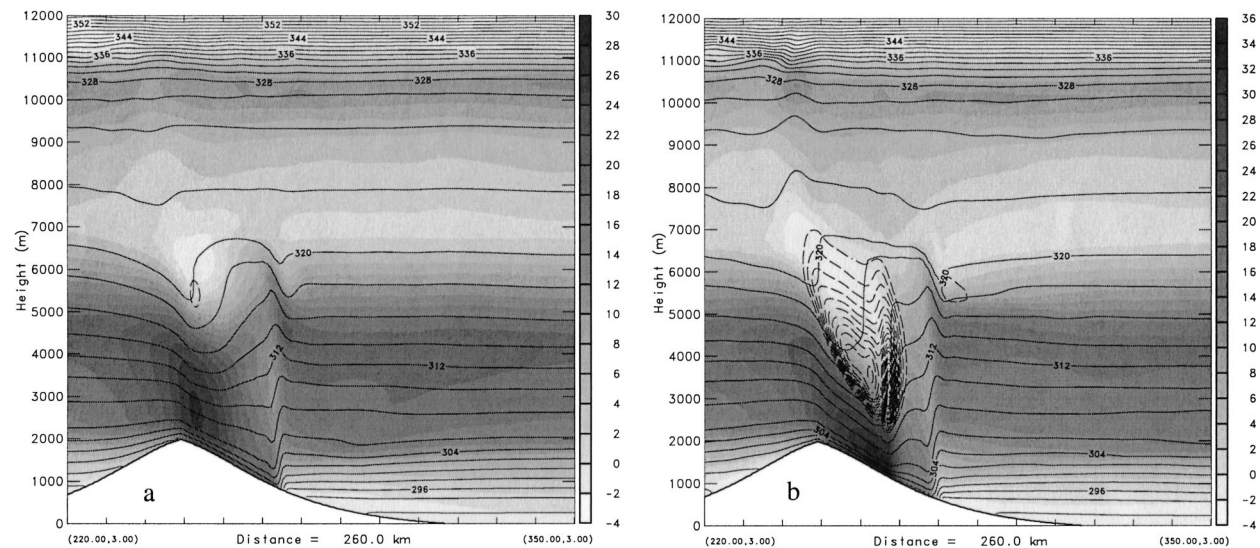


FIG. 18. Vertical cross section of potential temperature (contour interval = 2 K), wind speed (grayscale, m s^{-1}), and TKE (dashed contours, interval = $2 \text{ m}^2 \text{ s}^{-2}$) for the two-dimensional smooth terrain simulation (i.e., $h_s = 0$): (a) $t = 1.5 \text{ h}$; (b) $t = 3 \text{ h}$.

$\text{m}^2 \text{ s}^{-2}$ (Fig. 19a). The downslope wind maximum reaches 40 m s^{-1} . Correspondingly, there are two separate downslope wind speed cores located beneath the two TKE clusters. At $t = 3 \text{ h}$, there are three TKE clusters, one along the wave front, and the other two located above the lee slope (Fig. 19b). The maximum wind speed reaches 44 m s^{-1} in the two valleys. Compared with the $h_s = 0$ run, the hydraulic jump is about 20 km farther downstream.

A comparison between the two simulations illustrates the importance of smaller-scale terrain in mountain wave breaking and the development of strong downslope winds. Wave breaking develops much faster in the run with multiscale terrain. The corresponding turbu-

lence and downslope windstorm is significantly stronger. It is interesting that the second simulation captures distinct TKE peaks and downslope wind maxima as observed. Simulations using $k = 3, 4, 5, 6$ and $h_s = 100 \text{ m}, 200 \text{ m}$ indicate that even with $h_s = 100 \text{ m}$, the smaller-scale terrain tends to accelerate and enhance wave breaking, as well as the downslope windstorm. For $k \leq 4$ (i.e., a wavelength of 17.5 km), wave breaking develops faster and is more severe (i.e., larger TKE) with the increasing wavenumber. The surface drag at $t = 4 \text{ h}$ computed from seven simulations corresponding to $h_s = 300 \text{ m}$ and $k = 0-6$ is shown in Fig. 20.

The surface drag increases with increasing wavenumber until $k = 4$. The drag for $k = 4$ is more than twice

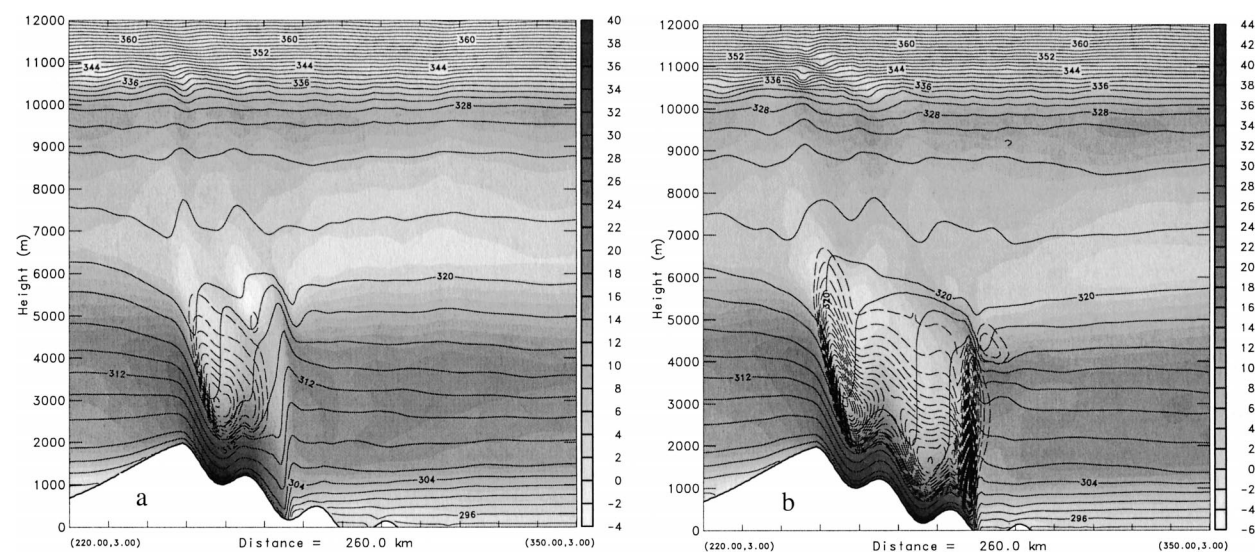


FIG. 19. Same as Fig. 18, except for $h_s = 300 \text{ m}$ and $k = 2$.

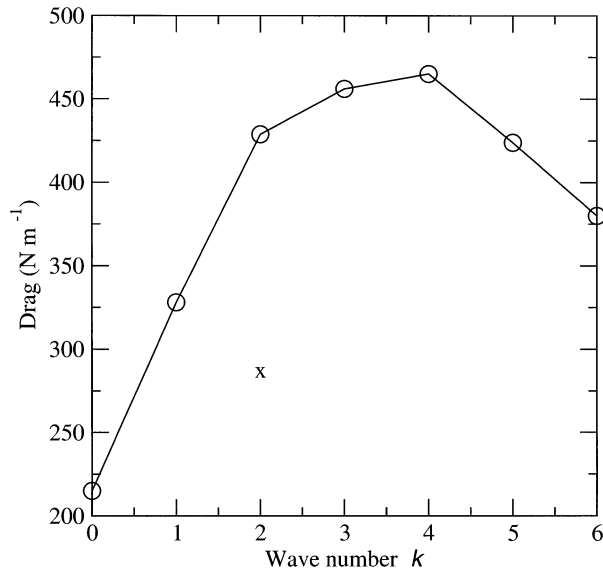


FIG. 20. The mountain drag derived from two-dimensional idealized simulations using $h_s = 300$ m at $t = 4$ h as a function of the small-scale terrain wavenumber k . The symbol "x" represents the drag computed from a run using $h_s = 100$ m and $k = 2$.

the value of the corresponding smooth terrain run (i.e., $k = 0$). The drag of the run using $h_s = 100$ m and $k = 2$ is significantly larger than the smooth terrain run as well. Further increase of the wavenumber causes the drag to decrease, likely due to wave dispersion as the nonhydrostatic component becomes dominant for shorter waves. For each simulation, the drag increases with integration time rapidly in the first 3 h and the evolution of drag with time is fairly slow after 4 h, associated with a quasi-steady state in the vicinity of the mountain. An identical plot with the drag derived from 12-h integrations (not shown) show the same trend qualitatively.

b. Mechanistic aspects

According to linear theory, wave energy launched from a bell-shaped mountain is proportional to the square of the mountain height, as is the mountain drag (e.g., for a bell-shaped two-dimensional mountain, $\text{drag} \propto U h_m^2$). Considering that the height of the smaller-scale terrain (i.e., ~ 300 m) is approximately one order of magnitude smaller than that of the large-scale terrain (i.e., ~ 2000 m), the linear contribution to the downslope winds and the total drag from the smaller-scale terrain should be insignificant. To show this, we conducted an idealized simulation with the identical setup as the pair of simulations shown in Figs. 18 and 19 except for $h_m = 0$ and $h_s = 300$ m. With the smaller-scale terrain embedded in the slow boundary layer flow, the wave response aloft is extremely weak (not shown). We repeated this simulation with the Vipiteno sounding truncated at the 1700-m level so that the mountain top wind

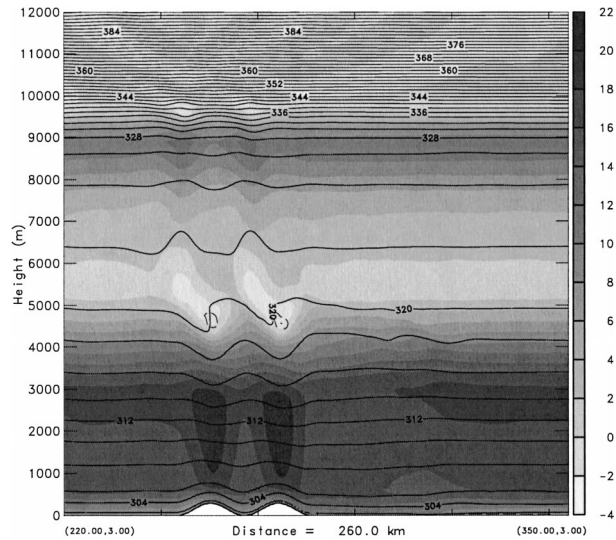


FIG. 21. Same as Fig. 18b, except that $h_m = 0$ and $h_s = 300$ m using a Vipiteno sounding that was truncated at the 1700-m level.

speed is the same as the two simulations shown in Figs. 18 and 19. As shown in Fig. 21, at $t = 3$ h, the wave breaking is confined to just below the critical level, and is much weaker than in the multiscale simulation. No strong downslope winds are observed.

Based on these simulations, we conclude that the significant enhancement of wave breaking, TKE generation, drag, and downslope winds by smaller-scale terrain is likely associated with nonlinear wave-wave interactions. The vertical group velocity of a stationary hydrostatic wave is approximately k/N , where k is the horizontal wavenumber (e.g., Smith 1979). Therefore, the shorter waves associated with the small-scale terrain likely break before the longer waves due to the faster vertical group velocity. The turbulent layer induced by the breaking shorter waves helps to reflect the long waves downward and therefore, promotes the amplification and subsequent breakdown of the long waves.

Furthermore, once the downslope windstorm develops, the shooting flow impinges on the small-scale terrain, and therefore, is able to launch larger-amplitude waves ($w \sim U$ near the ground). In return, the increased wave energy launched from the small-scale terrain reinforces the wave breaking aloft and downslope winds near the surface.

Although we are primarily interested in the transient features associated with wave breaking, a few integrations have been carried out to 12 h in order to assess the long-term behavior. For $t > 4$ h, the hydraulic jump front propagates downstream and leaves a quasi-steady state in the vicinity of the terrain. If the integration time is scaled using the advection time based on small-scale terrain wavelength (i.e., $T = U/L_s$, where L_s is the wave length of the small-scale terrain, and U is the mean wind speed between the boundary layer top and the critical

level), $t = 1.5, 3, 4, 12$ h approximately correspond to 3, 6, 8, and 24 nondimensional time units.

While these simulations are self-consistent and qualitatively agree with observations, it should be pointed out, however, that only a single sounding is used in our idealized simulations. Wave response to multiscale terrain forcing for a broader-parameter space is beyond the scope of this work. In the previous idealized simulations, surface friction was ignored and a free-slip boundary condition was applied. The results of several previous studies have suggested that wave breaking may be sensitive to bottom friction (e.g., Ólafsson and Bougeault 1997). Several additional simulations were performed with bottom friction and rotation. The turbulent vertical fluxes of horizontal momentum between the ground and the lowest grid point were computed following Mellor and Yamada (1974). The sounding used for the initial conditions was modified by increasing the wind speed below 2 km to 12 m s^{-1} , with a base state in geostrophic balance. These simulations indicate that bottom friction tends to slow down the propagation of the hydraulic jump front and weaken wave breaking. However, the enhancement of wave breaking, TKE generation, and downslope winds by the smaller-scale terrain is still evident, and qualitatively consistent with the previous free-slip bottom boundary condition simulations.

8. Conclusions

A breaking gravity wave event in the eastern Alps was observed on 21 October 1999 during the MAP special observational period (SOP). The characteristics and mechanisms for breaking wave induced by complex terrain were studied through analyzing observational data, diagnosing real-data simulations, and idealized modeling. The analysis of nearby soundings indicates that the occurrence of the wave breaking was associated with a critical level for meridional propagating waves, a layer of vertical wind shear in terms of both speed and direction, and a local Richardson number less than unity near the critical level. Previous theoretical and numerical studies suggest that the presence of a critical level or a small Richardson number layer in the ambient flow favors gravity wave breaking. The case presented in this study provides observational evidence in this regard.

The airborne lidar (SABL) reveals small-scale wave activity, large-scale flow descent, and high aerosol concentration in the boundary layer to the north of the Alps. The nearly uniformly deployed GPS dropsondes are shown to be very useful in the depiction of flow structure and wave activity below the flight level. Two vertical sections of along flight wind component, potential temperature, and turbulence are constructed by a manual analysis of the GPS dropsonde data and flight-level data. Downslope winds are observed with a maximum wind speed of 22 m s^{-1} , associated with strong flow descent over the lee slope of the Ötztaler Alpen. A deep hy-

draulic jump is identified associated with local convective instability, and a sudden transition from strong downslope winds to local wind reversal and turbulence. The hydraulic jump is tilted upstream with altitude similar to the observations of Boulder windstorm by Lilly and Zipser (1972) and propagates downstream during the observational period. The flow descent and ascent patterns are in agreement with the clear-cloudy patterns observed by the SABL. It should be noted that due to the limited number of dropsondes, the horizontal resolution is relatively coarse (20–40 km), and therefore, smaller-scale waves are not resolved. Additionally, the maximum leeside wind speed may be significantly underestimated due to insufficient sampling.

The flight-level data from the two transverses have been examined extensively. The vertical displacement of air particles along the flight track shows both smooth waves of wavelengths from 6–8 to 11 km and sharp wave shapes corresponding to highly nonlinear or breaking waves. The spectra of the high-frequency data of three velocity components indicate a possible turbulent inertial subrange with horizontal scales up to 5 km. Spectra for both transverses show multiple energy-containing peaks, indicative of a multiscale wave response to the complex terrain underneath. A peak at the 4.5-km wavelength is probably associated with eddies generated by gravity wave breaking.

The vertical fluxes of the zonal and meridional momentum along the flight track are positive and negative, respectively, during the two transverses. The heat flux associated with eddies (horizontal scales less than 5 km) along the first transverse is positive between 47° and 47.5°N , which indicates that the air is convectively unstable. Along the second transverse, the convectively unstable region propagates downstream and becomes more concentrated as indicated by a positive narrow maximum in the heat flux at 47.5°N . The downstream shift of the convectively unstable zone is consistent with the turbulent kinetic energy (TKE) distribution. For the first transverse, the TKE shows three spikes with the maximum located at 47.25°N . While the TKE along the second transverse also shows a three-spike structure, the maximum is located at 47.5°N and is significantly larger than the observed maximum along the first transverse. The width of individual TKE peaks is about 10–20 km. The TKE analysis also indicates that the turbulence at the flight level is highly nonisotropic along the first transverse with the contribution from the v -wind component dominant. However, the turbulence is primarily isotropic along the second transverse.

The COAMPS real-data simulation captures many of the observed characteristics of the flow, including the descent over the lee slope of the Ötztaler Alpen and the strong downslope winds near the surface. COAMPS also simulates the propagation and strengthening of the hydraulic jump. However, there are a number of observed features that the model is not able to simulate realistically such as the critical level and wave breaking near

the flight level. The simulated hydraulic jump is significantly weaker than that observed. These inadequacies suggest that the predictability of wave breaking over complex terrain may be limited by factors beyond simply the horizontal resolution, such as the initial and boundary condition, as well as the model dynamical formulation. The comparison between the observed and simulated Vipiteno soundings indicate that while COAMPS captures the strong southerly winds below 6 km ASL and reverse shear aloft, it does not adequately simulate the critical level. An idealized simulation is conducted with the two-dimensional bell-shaped terrain described in section 7 and the Vipiteno sounding derived from the COAMPS simulation to test the sensitivity of the wave breaking to the presence of the critical level. Although fairly strong downslope winds are simulated, in the absence of the critical level, the model fails to produce the wind reversal and TKE clusters as shown in Figs. 18b and 19b.

Two-dimensional simulations using the Vipiteno 0600 UTC sounding with idealized terrain have been performed to examine the significance of terrain spectrum in gravity wave breaking. The simulations are motivated by the complex terrain along the flight track and the multiscale flow response as indicated by the observational analysis. The idealized simulations capture some of the key observed features such as the strong downslope winds associated with lee descent, a propagating hydraulic jump with a narrow zone of concentrated TKE, and the backward tilt of the phase line. The comparisons between two simulations, that used smooth large-scale terrain and large-scale terrain with smaller-scale features superposed on the lee slope, indicate that the multiscale terrain promotes wave breaking, and further enhances downslope winds and turbulence generation. The simulations also suggest that orographic drag can be significantly enhanced by the presence of smaller-scale terrain.

Acknowledgments. This research was supported by the Office of Naval Research (ONR) program element 0601153N. The authors benefited from discussions with Drs. R. B. Smith, S. Wang, and Q. Wang. The authors also thank two anonymous reviewers for their constructive comments and suggestions. The data for the field program were collected in a joint effort by the MAP scientists and staff, especially our colleagues in the gravity wave breaking team: Drs. A. Broad, D. Fritts, V. Grubišić, K. Hoinka, J. Kuettner, G. Poulos, R. B. Smith, S. Smith, and H. Volkert. COAMPS is a trademark of the Naval Research Laboratory.

REFERENCES

- Afanasyev, Y. D., and W. R. Peltier, 1998: The three-dimensionalization of stratified flow over two-dimensional topography. *J. Atmos. Sci.*, **55**, 19–39.
- Bougeault, P., and Coauthors, 2001: The MAP special observing period. *Bull. Amer. Meteor. Soc.*, **82**, 433–462.
- Clark, T. L., and W. R. Peltier, 1977: On the evolution and stability of finite amplitude mountain waves. *J. Atmos. Sci.*, **34**, 1715–1730.
- , and R. D. Farley, 1984: Severe downslope windstorm calculations in two and three spatial dimensions using anelastic interactive grid nesting: A possible mechanism for gustiness. *J. Atmos. Sci.*, **41**, 329–350.
- , W. D. Hall, and R. M. Banta, 1994: Two- and three-dimensional simulations of the 9 January 1989 severe Boulder windstorm. Comparison with observations. *J. Atmos. Sci.*, **51**, 2317–2343.
- , R. M. Kerr, D. Middleton, L. Radke, F. Martin, P. J. Neiman, and D. Levinson, 2000: Origins of aircraft-damaging clear-air turbulence during the 9 December 1992 Colorado downslope windstorm: Numerical simulations and comparison with observations. *J. Atmos. Sci.*, **57**, 1105–1131.
- Doyle, J. D., and R. B. Smith, 2003: Mountain waves over the Hohe Tauern: Influence of upstream diabatic effects. *Quart. J. Roy. Meteor. Soc.*, **129**, 799–823.
- , and Coauthors, 2000: An intercomparison of model-predicted wave breaking for the January 11 1972 Boulder windstorm. *Mon. Wea. Rev.*, **128**, 901–914.
- Durran, D., 1986: Another look at downslope windstorms. Part I: On the development of analogs to supercritical flow in an infinitely deep, continuously stratified fluid. *J. Atmos. Sci.*, **43**, 2527–2543.
- , 1995: Do breaking mountain waves decelerate the local mean flow? *J. Atmos. Sci.*, **52**, 4010–4032.
- Fritts, D. C., 1978: The nonlinear gravity wave–critical level interaction. *J. Atmos. Sci.*, **35**, 397–413.
- , and M. J. Alexander, 2003: A review of gravity wave dynamics and effects in the middle atmosphere. *Rev. Geophys.*, **41**, 1–64.
- Georgelin, M., and F. Lott, 2001: On the transfer of momentum by trapped lee waves: Case of the IOP3 of PYREX. *J. Atmos. Sci.*, **58**, 3563–3580.
- Hines, C. O., 1968: Some consequences of gravity wave critical layers in the upper atmosphere. *J. Atmos. Terr. Phys.*, **30**, 837–843.
- Hodur, R. M., 1997: The Naval Research Laboratory's Coupled Ocean/Atmosphere Mesoscale Prediction System (COAMPS). *Mon. Wea. Rev.*, **125**, 1414–1430.
- Holton, J. R., 1982: The role of gravity wave induced drag and diffusion in the momentum budget of the mesosphere. *J. Atmos. Sci.*, **39**, 791–799.
- Karacostas, T. S., and J. D. Marwitz, 1980: Turbulent kinetic energy budget over mountainous terrain. *J. Appl. Meteor.*, **19**, 163–174.
- Kim, Y.-J., S. D. Eckermann, and H.-Y. Chun, 2003: An overview of the past, present, and future of gravity-wave drag parameterization for numerical climate and weather prediction models. *Atmos.–Ocean*, **41**, 65–98.
- Klemp, J. B., and D. K. Lilly, 1978: Numerical simulation of hydrostatic mountain waves. *J. Atmos. Sci.*, **35**, 78–107.
- Leovy, C., 1964: Radiative equilibrium of the mesosphere. *J. Atmos. Sci.*, **21**, 238–248.
- Lilly, D. K., and E. J. Zipser, 1972: The front range windstorm of 11 January 1972—A meteorological narrative. *Weatherwise*, **25**, 56–63.
- , and P. J. Kennedy, 1973: Observations of a stationary mountain wave and its associated momentum flux and energy dissipation. *J. Atmos. Sci.*, **30**, 1135–1152.
- , and J. B. Klemp, 1980: Comments on “The evolution and stability of finite-amplitude mountain waves. Part II: Surface wave drag and severe downslope windstorm.” *J. Atmos. Sci.*, **37**, 2119–2121.
- Lindzen, R. S., 1981: Turbulence and stress owing to gravity wave and tidal breakdown. *J. Geophys. Res.*, **86**, 9707–9714.
- Long, R. R., 1953: Some aspects of the flow of stratified fluids. Part I: A theoretical investigation. *Tellus*, **5**, 42–58.
- Mellor, G. L., and T. Yamada, 1974: A hierarchy of turbulence closure models for planetary boundary layers. *J. Atmos. Sci.*, **31**, 1–28.
- Miller, P. P., and D. R. Durran, 1991: On the sensitivity of downslope windstorms to the asymmetry of the mountain profile. *J. Atmos. Sci.*, **48**, 1457–1473.

- Ólafsson, H., and P. Bougeault, 1997: The effect of rotation and surface friction on orographic drag. *J. Atmos. Sci.*, **54**, 193–210.
- Peltier, W. R., and T. L. Clark, 1979: The evolution and stability of finite amplitude mountain waves. Part II: Surface wave drag and severe downslope winds. *J. Atmos. Sci.*, **36**, 1498–1529.
- , and —, 1980: Reply. *J. Atmos. Sci.*, **37**, 2122–2125.
- , and —, 1983: Nonlinear mountain waves in two and three spatial dimensions. *Quart. J. Roy. Meteor. Soc.*, **109**, 527–548.
- Ralph, F. M., and P. L. Neiman, 1997: Lidar observations of a breaking mountain wave associated with extreme turbulence. *Geophys. Res. Lett.*, **24**, 663–666.
- Rottman, J. W., and R. B. Smith, 1989: A laboratory model of severe downslope winds. *Tellus*, **41A**, 401–415.
- Smith, R. B., 1979: The influence of mountains on the atmosphere. *Advances in Geophysics*, Vol. 21, Academic Press, 87–230.
- , 1985: On severe downslope winds. *J. Atmos. Sci.*, **42**, 2597–2603.
- , S. Skubis, J. D. Doyle, A. S. Broad, C. Kiemle, and H. Volkert, 2002: Mountain waves over Mont Blanc: Influence of a stagnant boundary layer. *J. Atmos. Sci.*, **59**, 2073–2092.
- Volkert H., C. Keil, C. Kiemle, G. Poberaj, J.-P. Chaboureaud, and E. Richard, 2003: Gravity waves over the eastern Alps: A synopsis of the 25 October 1999 event (IOP-10) combining in-situ and remote sensing measurements with a high-resolution simulation. *Quart. J. Roy. Meteor. Soc.*, **129**, 777–797.